



# Fabrication and nucleation study of $\beta$ -PbO<sub>2</sub>-Co<sub>3</sub>O<sub>4</sub> OER energy-saving electrode

Shiwei He<sup>1,2</sup> · Ruidong Xu<sup>3</sup> · Yuqing Guo<sup>4</sup> · Zhuo Zhao<sup>2</sup>  · Bohao Yu<sup>3</sup> · Saijun Xiao<sup>2</sup> · Huihong Lv<sup>1</sup>

© Springer Nature Switzerland AG 2019

## Abstract

In this study,  $\beta$ -PbO<sub>2</sub>-Co<sub>3</sub>O<sub>4</sub> composite coatings were synthesized on a substrate using the electrodeposition method in an electrolyte containing Pb<sup>2+</sup> and Co<sub>3</sub>O<sub>4</sub> particles. The preparation process study shows that the  $\beta$ -PbO<sub>2</sub> bath containing Co<sub>3</sub>O<sub>4</sub> particles becomes more stable for an ultrasonic dispersion time within 30 min, with the stability beginning to decrease after the ultrasonic time exceeds 30 min. Co<sub>3</sub>O<sub>4</sub> particles in the  $\beta$ -PbO<sub>2</sub> bath are positively charged, with anions being adsorbed onto the particles. The nucleation behavior study shows that the electric field force plays a dominant role in the adsorption process for the Co<sub>3</sub>O<sub>4</sub> particles. The nucleation and growth of  $\beta$ -PbO<sub>2</sub> on the Co<sub>3</sub>O<sub>4</sub> particles started for the particles closer to the substrate. In addition, the thickness of the  $\beta$ -PbO<sub>2</sub> layer on the Co<sub>3</sub>O<sub>4</sub> particles was inversely proportional to the distance between the Co<sub>3</sub>O<sub>4</sub> particles and the substrate. Compared to the pure PbO<sub>2</sub> electrode, the oxygen evolution overpotentials for the  $\beta$ -PbO<sub>2</sub>-Co<sub>3</sub>O<sub>4</sub> electrode are decreased significantly, which demonstrates an energy-saving effect.

**Keywords** Co<sub>3</sub>O<sub>4</sub> ·  $\beta$ -PbO<sub>2</sub> · OER · Nucleation

## 1 Introduction

The oxygen evolution reaction (OER) is an important reaction in modern industry. This reaction plays an important role in hydrogen production, electro-organic syntheses, and metal electrowinning processes. OER requires the distribution of four redox processes: the coupling of multiple proton and electron transfers, and the formation of two O-O bonds [1]. In an electrochemical system, OER occurs at high positive potentials when aqueous solution is used as the electrolyte. The slow reaction kinetics due to the involvement of four electrons in the reaction mechanism is the main obstacle of OER. As OER is the primary reaction at the anode, a large amount of the energy in the electrochemical system will be dedicated to it. Therefore, the continued development of catalysts with low overpotential

and fast reaction kinetics with high stability to improve OER efficiency remains a scientific and technological challenge [2, 3].

Coated electrodes are now extensively used in the electrochemical field because they have both the mechanical properties of the substrate and the electrochemical properties of the coating. As one of the more traditional coatings, lead dioxide (PbO<sub>2</sub>) has attracted considerable attention due to its demonstrated advantages, including low electrical resistivity, low cost, ease of preparation, good chemical stability, and relatively large surface area [4–7]. Thus, lead dioxide has already been used in waste water treatment [8–10], ozone generation [11, 12], lead-acid batteries [13–15], analytical sensors [16], and the metal electrowinning process [17]. It is well-known that PbO<sub>2</sub> shows two phases: the  $\alpha$  phase and  $\beta$  phase. Electrodeposition is a traditional way

✉ Zhuo Zhao, ahutyouse03@163.com | <sup>1</sup>Key Laboratory of Metallurgical Emission Reduction and Resources Recycling, Ministry of Education, Maanshan 243002, China. <sup>2</sup>School of Metallurgical Engineering, Anhui University of Technology, Maanshan 243002, China. <sup>3</sup>State Key Laboratory of Complex Nonferrous Metal Resources Cleaning Utilization, Kunming 650093, China. <sup>4</sup>College of Chemistry, Chemical Engineering and Biotechnology, Donghua University, Shanghai 201620, China.



to prepare these two phases of  $\text{PbO}_2$  [18]. The conditions (primarily composition and temperature) of the synthesizing bath determine the phase of the deposited material [19]. To the best of our knowledge, the electrochemical activity and electrical conductivity of  $\beta\text{-PbO}_2$  is better than that of  $\alpha\text{-PbO}_2$  [20]. However, as an interlayer of the electrode, the binding force for  $\beta\text{-PbO}_2$  and its underlayer can be improved by using  $\alpha\text{-PbO}_2$  [21].

The OER is sensitive to the intrinsic structure of the catalysts [22]. It has been demonstrated that conductive transition metal oxides can promote the OER with high efficiency and current density in either highly acidic or highly alkaline solutions [23]. Among these metal oxides,  $\text{Co}_3\text{O}_4$  shows excellent catalytic activity and with a lower cost.  $\text{Co}_3\text{O}_4$  is a p-type semiconductor material with a spinel structure, which is coordinated by  $\text{Co}^{2+}$  in a tetrahedron and  $\text{Co}^{3+}$  in an octahedron [24]. Due to its high capacity ( $\sim 890 \text{ mAh/g}$ ), good redox reversibility, strong corrosion resistance, low price, and environmental friendliness,  $\text{Co}_3\text{O}_4$  has been widely used for catalysis, gas sensors, lithium batteries, and capacitors [25–32]. As one of the high catalytic activity metal oxides,  $\text{Co}_3\text{O}_4$  was incorporated into the  $\text{PbO}_2$  matrix to improve the reaction rate of the oxygen evolution process [33]. However,  $\text{PbO}_2$  composite coatings containing  $\text{Co}_3\text{O}_4$  particles were found to be considerably rougher compared to the pure  $\text{PbO}_2$  coatings, which may be caused by the preferred orientation change in the crystal growth process [34].

In this study,  $\beta\text{-PbO}_2\text{-Co}_3\text{O}_4$  composite coatings were synthesized on a substrate using the electrodeposition method in an electrolyte containing  $\text{Pb}^{2+}$  and  $\text{Co}_3\text{O}_4$  particles. To improve the binding force of the substrate and the  $\beta\text{-PbO}_2\text{-Co}_3\text{O}_4$  outer layer, the substrates were covered with an  $\alpha\text{-PbO}_2$  layer via electrodeposition pretreatment. The influence of the preparation parameters for the composite coating, such as ultrasonic dispersion time and particle concentration of the electrolyte, was investigated using a Zeta potential test and anodic polarization test. The morphology and structure of the  $\beta\text{-PbO}_2\text{-Co}_3\text{O}_4$  composite layer for varying nucleation times was measured using XRD, SEM, and EDS. To the best of our knowledge, the nucleation process for the  $\beta\text{-PbO}_2\text{-Co}_3\text{O}_4$  composite on the surface of the  $\alpha\text{-PbO}_2$  layer has not been thoroughly elucidated to date. In addition, several of the conclusions obtained in this study can explain the unusual roughness of the  $\beta\text{-PbO}_2\text{-Co}_3\text{O}_4$  composite.

## 2 Experimentation

### 2.1 Materials and reagents

A Pb–0.3%Ag alloy plate with dimensions of  $40 \text{ mm} \times 20 \text{ mm} \times 2 \text{ mm}$  was selected as the substrate. All

chemicals were of analytical grade and purchased from Aladdin Industrial Corporation (Shanghai, China). All solutions were prepared by using deionized water supplied from an EPED water purification system. Bath solutions were prepared by dissolving  $\text{Pb}(\text{NO}_3)_2$  in  $\text{HNO}_3$  solution. The concentrations of  $\text{Pb}^{2+}$  and  $\text{HNO}_3$  were controlled at 0.8 M and 0.2 M, respectively.

### 2.2 Electrode preparation

The  $\text{Co}_3\text{O}_4$  doped  $\beta\text{-PbO}_2$  electrode consisted of a Pb–0.3%Ag alloy substrate,  $\alpha\text{-PbO}_2$  inter layer, and  $\beta\text{-PbO}_2\text{-Co}_3\text{O}_4$  outer layer. First, the Pb–0.3%Ag alloy substrates were pretreated by polishing, degreasing, and acid etching. Second, the  $\alpha\text{-PbO}_2$  inter layer was electrodeposited in alkaline solution, which consisted of 3 M NaOH and 0.15 M Pb(II). The current density and temperature was controlled at  $13.5 \text{ mA/cm}^2$  and  $40^\circ\text{C}$ , respectively. The  $\beta\text{-PbO}_2$  plating bath consisted of 0.2 M  $\text{HNO}_3$  + 0.8 M  $\text{Pb}^{2+}$  with varying concentrations of  $\text{Co}_3\text{O}_4$  particles. Figure 1 shows a schematic diagram for the electrode preparation device. The substrate was contacted to the anode and the stainless steel plates were contacted to the cathode.

### 2.3 Zeta potential and particle size test

The Zeta potential and particle size was measured by analyzing  $\text{Co}_3\text{O}_4$  (0.1 g) in solution (10 ml) using the ZetaPALS (Brookhaven). All samples were sonicated for 0–50 min before Zeta potential measurements. The frequency and power of the ultrasonicator was controlled at 40 kHz and 300 W, respectively. The Zeta potential was measured from the electrophoretic mobility obtained using the Smoluchowski equation.

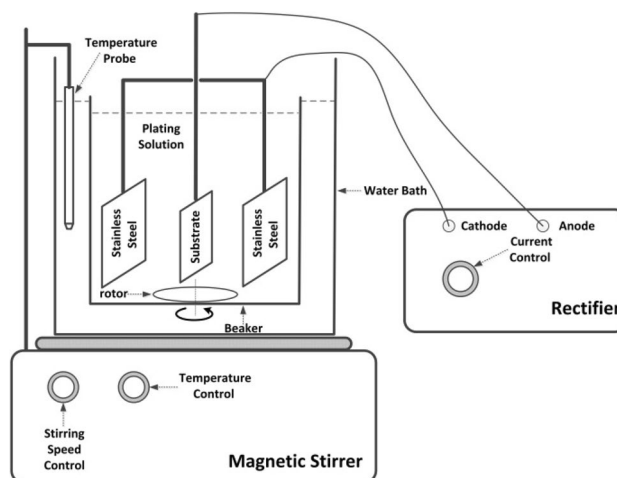


Fig. 1 Schematic diagram for the electrode preparation device

## 2.4 Anodic polarization curve measurement

The anodic polarization curves were obtained in a synthetic zinc electro-winning simulated electrolyte composed of 50 g/L  $\text{Zn}^{2+}$  (added as  $\text{ZnSO}_4$ ) and 150 g/L  $\text{H}_2\text{SO}_4$ , at 35 °C. The scan rates were controlled at 5 mV/s. All of the electrochemical measurements were conducted using a PARSTAT2273 electrochemical workstation with a three-electrode system. The working electrode with an effective area of 1 cm<sup>2</sup> was first treated by wax-sealing. The reference electrode was a saturated calomel electrode (SCE), and the counter electrode was a graphite electrode. The reference electrode and working electrode were linked by a Luggin capillary filled with agar and potassium chloride. In addition, the distance between the capillary and working electrode surface was approximately 2d (d is the diameter of the capillary) with d = 0.5 mm.

## 2.5 Characterization of the surface and phase composition

The phase composition and surface microstructure characteristics for the  $\text{PbO}_2$  composite layer were measured by a D/Max-2200 X-ray diffractometer (XRD) and Nova NanoSEM450 scanning electron microscope (SEM), respectively.

# 3 Results and discussion

## 3.1 Zeta potential measurement for the electrolyte

The Zeta potential and particle size measured in a solution of 0.2 M  $\text{HNO}_3$  + 0.8 M  $\text{Pb}^{2+}$  with different ultrasonic dispersion time are shown in Fig. 2. The measured particle size was reduced from 7.86 to 2.63  $\mu\text{m}$  for an ultrasonic dispersion time of 20 min, which indicates a significant decrease. Following this decrease, the particle size was stabilized at approximately 2.7  $\mu\text{m}$ . This phenomenon is observed because the particles with larger size gradually sank to the bottom of the containing vessel in the first 20 min. The blue line shows the Zeta potential value along with the ultrasonic dispersion time. The Zeta potential value for the  $\text{Co}_3\text{O}_4$  particles in this solution gradually increased from 0 to 30 min. When the ultrasonic dispersion time exceeded 30 min, the value for the Zeta potential started to decrease. The absolute value of the Zeta potential is mainly used to characterize the stability of the solution. A greater absolute value for the Zeta potential indicates a more stable solution [35, 36]. Therefore, the  $\beta\text{-PbO}_2$  bath containing  $\text{Co}_3\text{O}_4$  particles becomes more stable for an ultrasonic dispersion time within 30 min, with the stability beginning to decrease after the ultrasonic time exceeds 30 min. In

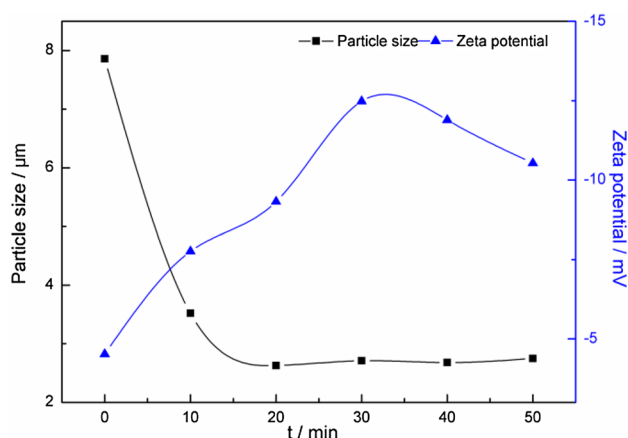


**Fig. 2** Particle size and Zeta potential for  $\text{Co}_3\text{O}_4$  particles in a  $\beta\text{-PbO}_2$  plating bath at different ultrasonic dispersion time

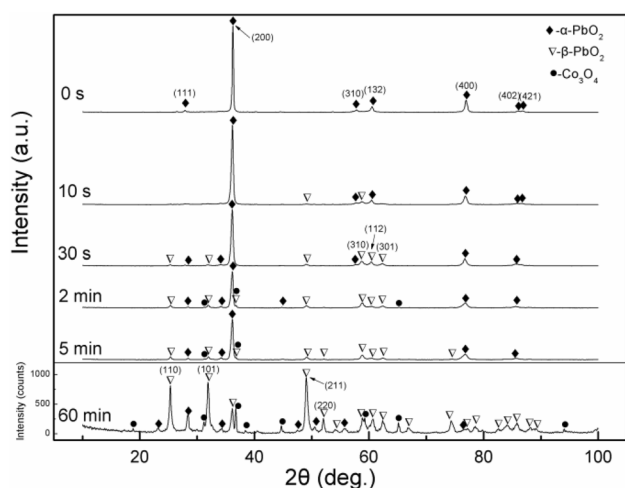
addition, the Zeta potential values are negative in all the ultrasonic time ranges, indicating that  $\text{Co}_3\text{O}_4$  particles are positively charged and that anions are adsorbed onto the particles. Considering the variation law for the particle size and Zeta potential with ultrasonic time, an ultrasonic dispersion time of 30 min is more suitable.

## 3.2 Nucleation of the composite layer

The substrates discussed in this section are  $\text{Pb-0.3\%Ag}/\alpha\text{-PbO}_2$ , with all of the studies on the nucleation process being conducted for the surface of the  $\alpha\text{-PbO}_2$  interlayer. In the nucleation study, the oxygen evolution reaction energy-saving (OERES) electrodes were prepared in a  $\beta\text{-PbO}_2$  bath with a  $\text{Co}_3\text{O}_4$  particle concentration of 15 g/L. The OERES electrodes were obtained using six different electrodeposition time of 0 s, 10 s, 30 s, 2 min, 5 min and 60 min. The XRD patterns for the OERES electrodes prepared at six different electrodeposition time are shown in Fig. 3. Figures 4, 5, 6 and 7 shows the SEM images and EDS analysis for the OERES electrodes prepared at different electrodeposition time.

It can be seen from Fig. 3 that the XRD pattern at a deposition time of 0 s is actually the diffraction pattern of the substrate; thus, the primary component is  $\alpha\text{-PbO}_2$ , with the  $\alpha\text{-PbO}_2$  crystal being preferentially crystallized on the (200) crystal plane. When the deposition time was 10 s, the main phase is still  $\alpha\text{-PbO}_2$ , but its diffraction intensity at the (200) plane becomes weak. In addition, there are two peaks for  $\beta\text{-PbO}_2$  with low diffraction intensity. According to the SEM images in Fig. 4, the  $\beta\text{-PbO}_2$  crystal grains basically cover the surface of the substrate at a deposition time of 10 s. However, since the XRD has a certain depth of penetration, the reflected phase information is still based on the substrate material. When the deposition

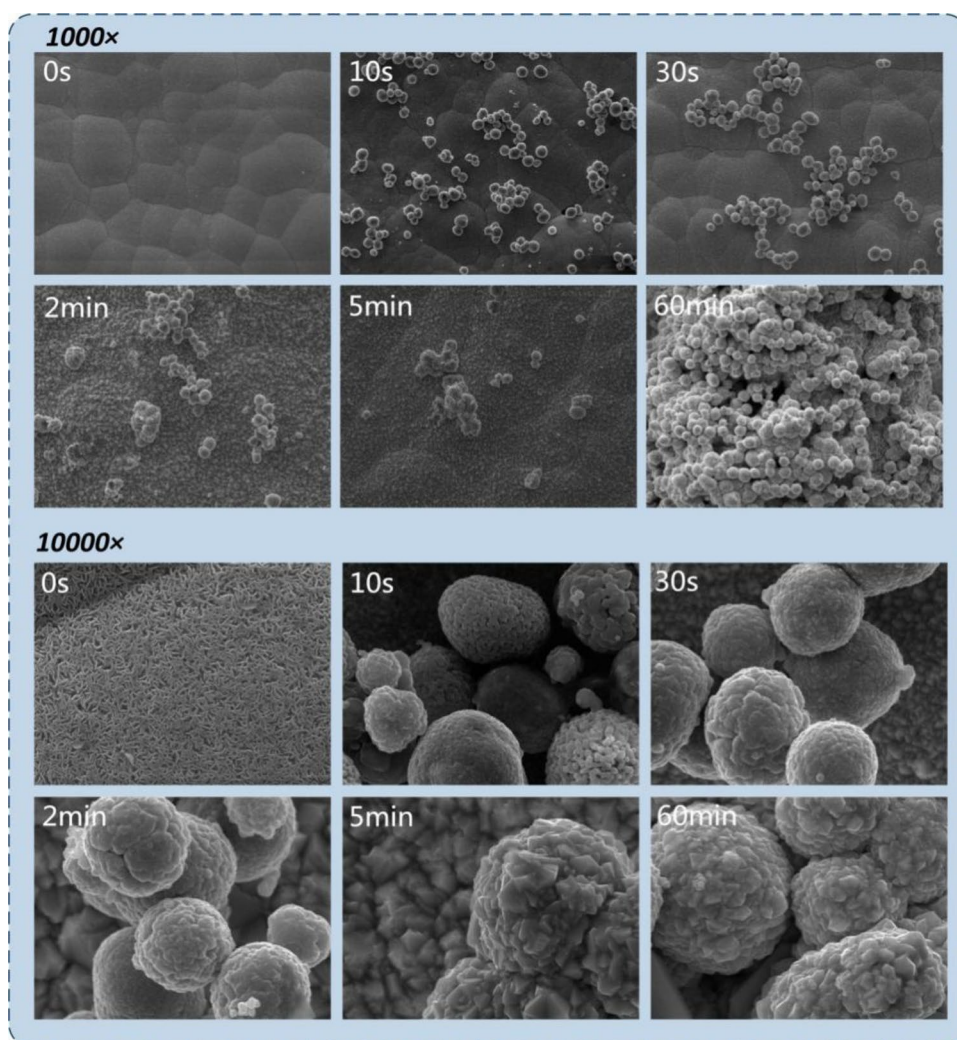




**Fig. 3** XRD patterns for OERES electrodes obtained at different deposition time

time was 30 s, the main phase of the XRD pattern is still  $\alpha$ -PbO<sub>2</sub>, and its diffraction intensity at the (200) crystal plane is further reduced. In addition, although the intensity of the  $\beta$ -PbO<sub>2</sub> diffraction peak is not high, the number of  $\beta$ -PbO<sub>2</sub> peaks increases significantly. For a deposition time of 2 min, the main phases are  $\alpha$ -PbO<sub>2</sub> and  $\beta$ -PbO<sub>2</sub>. The diffraction intensity for  $\alpha$ -PbO<sub>2</sub> in the (200) crystal plane continues to decrease, and the intensity and quantity of the  $\beta$ -PbO<sub>2</sub> characteristic peaks are similar to those found at 30 s. Moreover, a small amount of Co<sub>3</sub>O<sub>4</sub> diffraction peaks were captured during this deposition time. When the deposition time was 5 min, the XRD pattern does not notably change compared with the sample obtained using a deposition time of 2 min. The diffraction peak for  $\alpha$ -PbO<sub>2</sub> does not change significantly. The quantity of the  $\beta$ -PbO<sub>2</sub> diffraction peak continues to increase, but the intensity does not show a clear change. When the deposition time was extended to 60 min, the XRD pattern changed very clearly. The main phase was changed to  $\beta$ -PbO<sub>2</sub>, with a clear preferred crystal orientation for  $\beta$ -PbO<sub>2</sub> on the (211),

**Fig. 4** SEM images for OERES electrodes obtained at different deposition time (1000 $\times$ , 10,000 $\times$ )



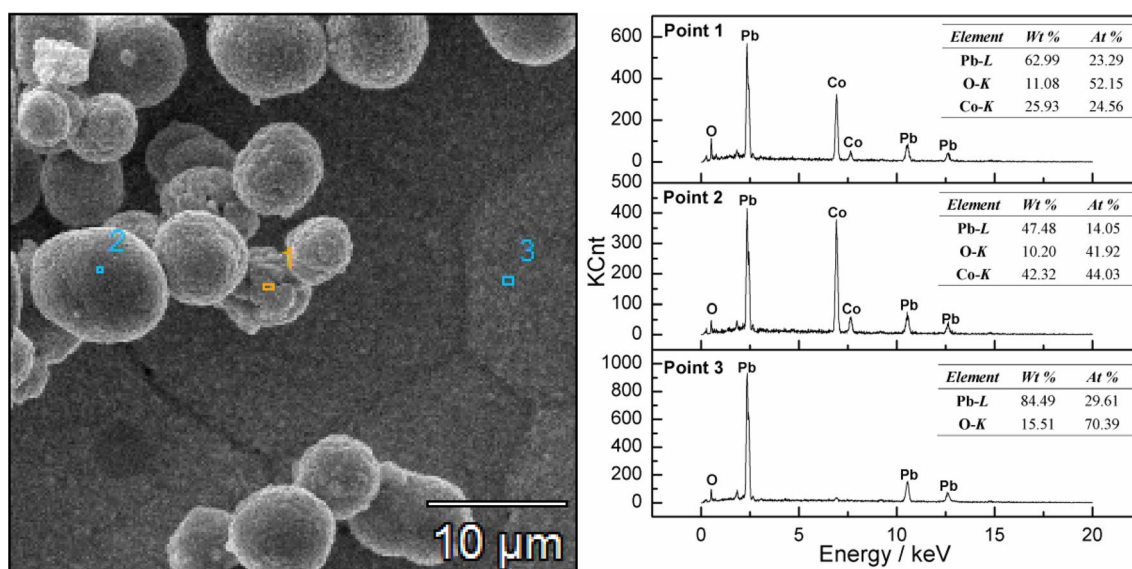


**Fig. 5** Energy spectrum analysis for the OERES electrodes for 10 s of electrodeposition

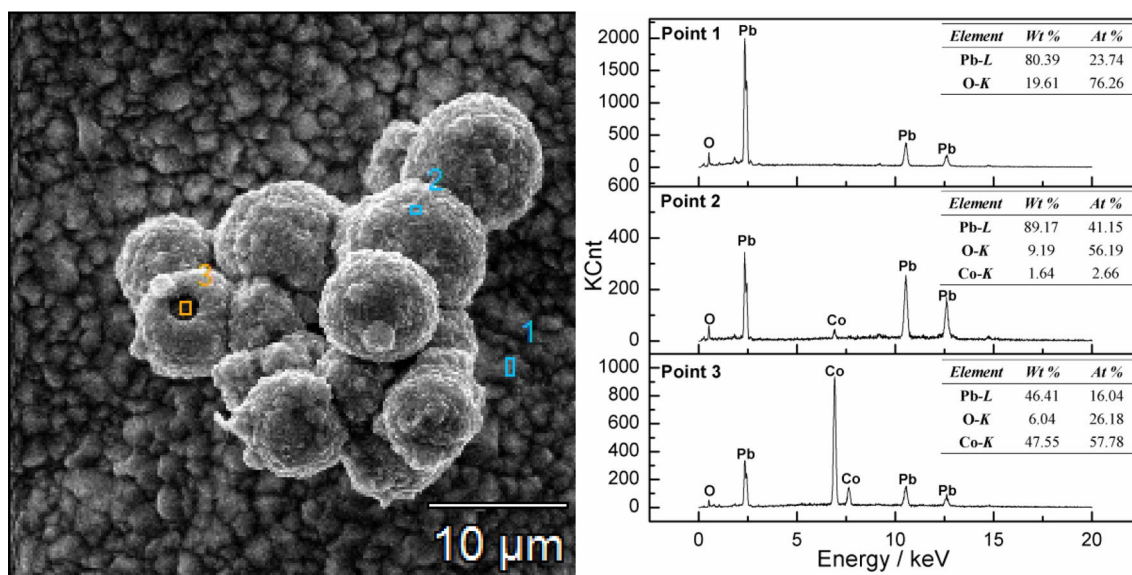


**Fig. 6** Energy spectrum analysis for OERES electrodes for 5 min of electrodeposition

(101) and (110) crystal planes. In addition, the diffraction peaks for  $\text{Co}_3\text{O}_4$  can be clearly detected in the composite deposition layer. However, since  $\text{Co}_3\text{O}_4$  enters the deposition layer using co-deposition methods, the content is not very high and the intensity of the diffraction peak is still at a low level. In summary, as the deposition time is extended, the intensity and number of  $\alpha\text{-PbO}_2$  diffraction peaks show a decreasing trend, while the intensity and number of  $\beta\text{-PbO}_2$  diffraction peaks show a gradually increasing trend. For a deposition time of 2 min, a diffraction peak for  $\text{Co}_3\text{O}_4$  was detected for the first time.

It can be seen from Fig. 4 that the morphology of the substrate is evident for a deposition time of 0 s. The  $\alpha\text{-PbO}_2$  substrate is composed of circular cells: the circular cell boundaries are clear, with the cell consisting of interwoven rod-shaped crystal grains. For a deposition time of 10 s, the circular shape of the  $\alpha\text{-PbO}_2$  substrate is still visible, but a layer of  $\beta\text{-PbO}_2$  nucleus has formed on the surface, with some positions for the circular cell boundaries not yet fully covered with a  $\beta\text{-PbO}_2$  nucleus. This shows that the nucleation of  $\beta\text{-PbO}_2$  on the substrate begins with the protrusion of the  $\alpha\text{-PbO}_2$  circular cell and gradually spreads to

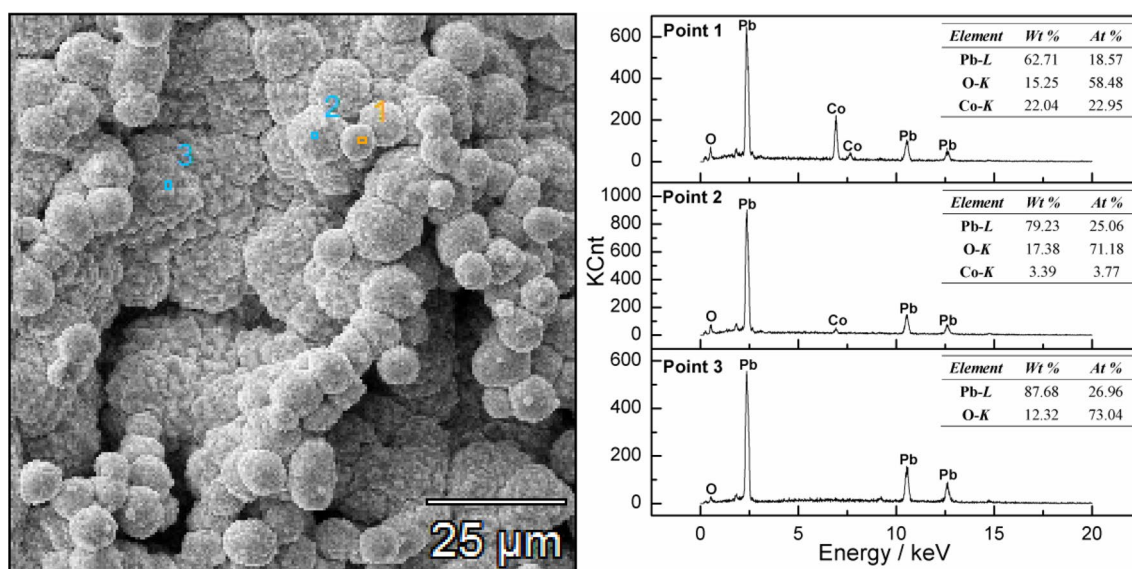


**Fig. 7** Energy spectrum analysis for OERES electrodes for 60 min of electrodeposition

the cell boundaries. In addition, a large number of spherical  $\text{Co}_3\text{O}_4$  particles are adsorbed onto the surface of the sediment layer. These particles are preferentially gathered at the boundaries of the circular cell. The cell boundaries of  $\alpha\text{-PbO}_2$  is the position that closer to the power source and thus the electric field force is stronger. In addition, the Zeta potential for the  $\text{Co}_3\text{O}_4$  particles in the bath is negative, which has already been demonstrated previously. Thus, the  $\text{Co}_3\text{O}_4$  particles with anions adsorbed are affected by the electric field force, leading to preferential adsorption onto the cell boundaries of the  $\alpha\text{-PbO}_2$  substrate. The analysis indicates that the electric field force around the substrate plays a dominant role in the adsorption of  $\text{Co}_3\text{O}_4$  particles. Due to this preferential adsorption, a large number of  $\text{Co}_3\text{O}_4$  particles gathered together in the cell boundaries. Moreover, the morphologies of the adsorbed particles and the original  $\text{Co}_3\text{O}_4$  particles are identical, indicating that no  $\beta\text{-PbO}_2$  is electro-crystallized onto the surface of the particles although some  $\text{Co}_3\text{O}_4$  particles have already been adsorbed onto the substrate. It can be concluded that the main process occurring during the deposition time of 0–10 s was nucleation of the  $\beta\text{-PbO}_2$  grains and adsorption of  $\text{Co}_3\text{O}_4$  particles.

Figure 5 shows the spot scanning energy spectrum for the OERES electrode prepared using a deposition time of 10 s. Point 1 is positioned on the  $\text{Co}_3\text{O}_4$  particles close to the substrate, point 2 is positioned on the  $\text{Co}_3\text{O}_4$  particles far from the substrate, and point 3 is positioned on the  $\beta\text{-PbO}_2$  deposition layer without  $\text{Co}_3\text{O}_4$  particles core. Comparing the composition of point 1 and point 2, the Pb content at point 1 is higher than that at point 2, and the Co content is lower than that at point 2, indicating a thicker

$\beta\text{-PbO}_2$  deposition layer on the  $\text{Co}_3\text{O}_4$  particles close to the substrate. This finding is attributable to the longer growth time of the  $\beta\text{-PbO}_2$  grains on the  $\text{Co}_3\text{O}_4$  particles closer to the substrate. Conversely, the  $\text{Co}_3\text{O}_4$  particles farther from the substrate have a shorter adsorption time; thus, the  $\beta\text{-PbO}_2$  crystal grains have a shorter time for nucleation and growth on the surface. Therefore, the  $\beta\text{-PbO}_2$  layer on the  $\text{Co}_3\text{O}_4$  particles farther from the substrate is thinner.

For a deposition time of 30 s, the circular shape of the  $\alpha\text{-PbO}_2$  is still visible. Moreover, the  $\beta\text{-PbO}_2$  crystal grains completely covered the surface of the substrate and begin to grow. In addition, fine  $\beta\text{-PbO}_2$  grains appeared on the  $\text{Co}_3\text{O}_4$  particles closest to the surface of the substrate;  $\beta\text{-PbO}_2$  grains do not appear on the  $\text{Co}_3\text{O}_4$  particles far from the surface of the substrate. It is indicated that the main process occurring during a deposition time of 10–30 s was the growth of  $\beta\text{-PbO}_2$  grains on the substrate and the nucleation of  $\beta\text{-PbO}_2$  grains on the  $\text{Co}_3\text{O}_4$  particles. For a deposition time of 2 min, the circular shape of the  $\alpha\text{-PbO}_2$  substrate has basically disappeared, with the  $\beta\text{-PbO}_2$  crystal grains continuing to grow. Moreover, the grain size for  $\beta\text{-PbO}_2$  on  $\text{Co}_3\text{O}_4$  particles was not significantly different from that observed at 30 s. This shows that for a deposition time of 30 s–2 min, the main process occurring at the electrode is the growth of  $\beta\text{-PbO}_2$  crystal grains on the substrate.

When the deposition time was 5 min, the grain size for  $\beta\text{-PbO}_2$  on  $\text{Co}_3\text{O}_4$  particles clearly grows, while the  $\beta\text{-PbO}_2$  grain size on the substrate does not show obvious changes. This shows that for a deposition time of 2–5 min, the main process occurring at the electrode is the growth of  $\beta\text{-PbO}_2$  grains on the  $\text{Co}_3\text{O}_4$  particles. Figure 6 shows



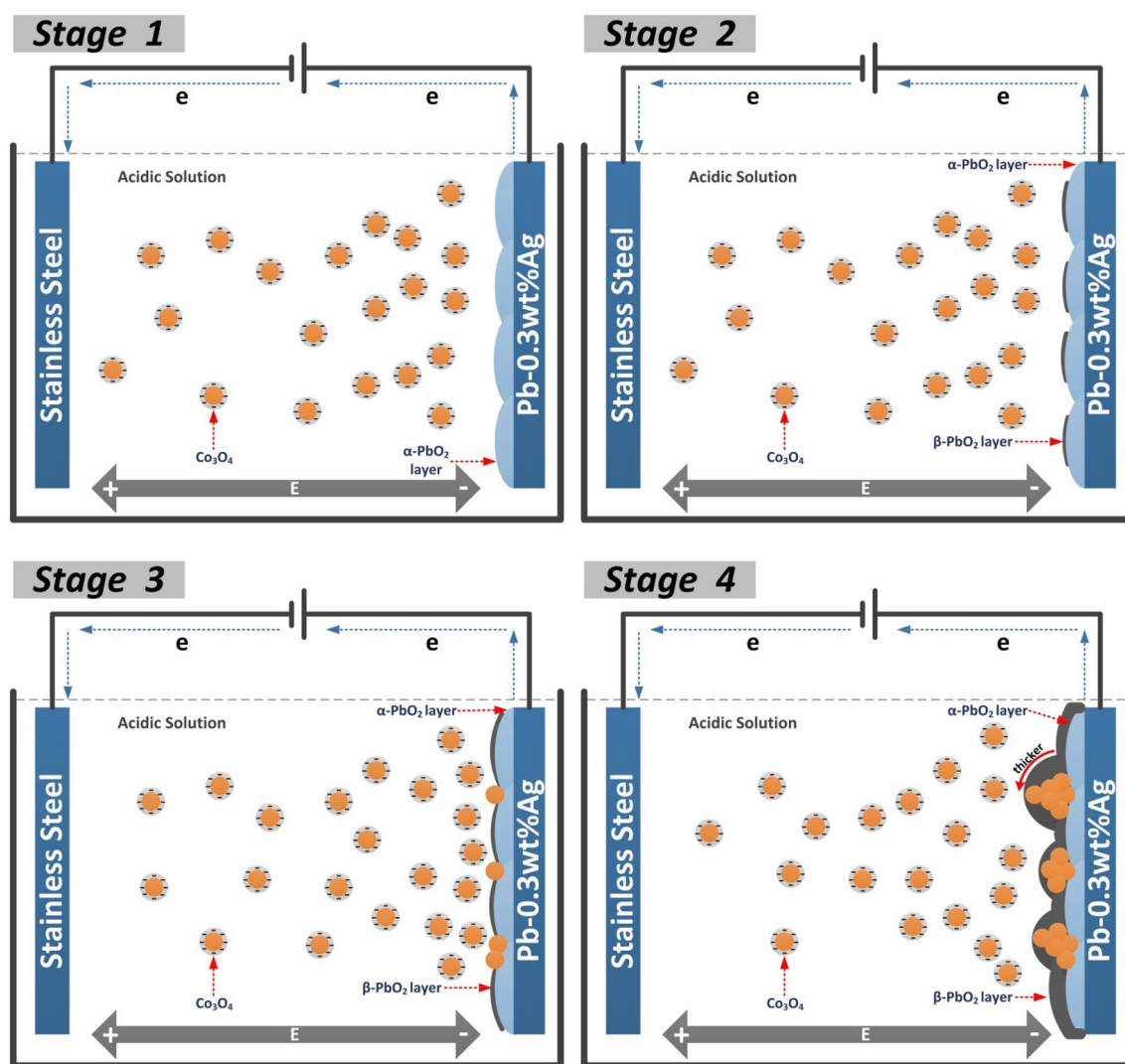


**Fig. 8** Nucleation model of  $\beta$ - $\text{PbO}_2$ - $\text{Co}_3\text{O}_4$  coating

the spot scanning energy spectrum for the OERES electrode prepared using a deposition time of 5 min. Point 1 is positioned on the  $\beta$ - $\text{PbO}_2$  deposition layer without core  $\text{Co}_3\text{O}_4$  particles, point 2 is positioned on  $\text{Co}_3\text{O}_4$  particles completely covered by  $\beta$ - $\text{PbO}_2$ , and point 3 is positioned on  $\text{Co}_3\text{O}_4$  particles not fully covered by  $\beta$ - $\text{PbO}_2$ . Comparing points 2 and 3, the Co element content at point 2 is much lower than that at point 3, while the content of Pb at point 2 is higher than that at point 3. It can be inferred that the position of point 3 is a gap in the  $\beta$ - $\text{PbO}_2$ -coated  $\text{Co}_3\text{O}_4$  particles, with the gap gradually closing, similar to point 2, during the deposition process. From the point 2 of Fig. 6 and point 1 of Fig. 5, it can be found that following extension of the deposition time to 5 min, the Pb content of the coated particles became higher and the Co content decreased, indicating that the  $\beta$ - $\text{PbO}_2$  layer on the coated

$\text{Co}_3\text{O}_4$  particles was significantly thickened at this time, which confirms the analysis based on Fig. 4.

When the deposition time was extended to 60 min, the grain size for  $\beta$ - $\text{PbO}_2$  on the substrate increased, but the grain size for  $\beta$ - $\text{PbO}_2$  on the  $\text{Co}_3\text{O}_4$  particles did not show a significant increase. From SEM photographs taken at low magnification, it can be seen that  $\text{Co}_3\text{O}_4$  particles are aggregated on the surface, with very serious agglomeration observed. This shows that for a deposition period of 5–60 min, the main process occurring at the electrode is the growth of  $\beta$ - $\text{PbO}_2$  grains on the substrate, continuous adsorption of  $\text{Co}_3\text{O}_4$  particles, and deposition of  $\beta$ - $\text{PbO}_2$  onto the surface of the  $\text{Co}_3\text{O}_4$  particles.

Figure 7 shows the spot scanning energy spectrum for the OERES electrode prepared using a deposition time of 60 min. Point 1 is positioned on the  $\text{Co}_3\text{O}_4$  particle farther from the substrate, point 2 is positioned on the  $\text{Co}_3\text{O}_4$

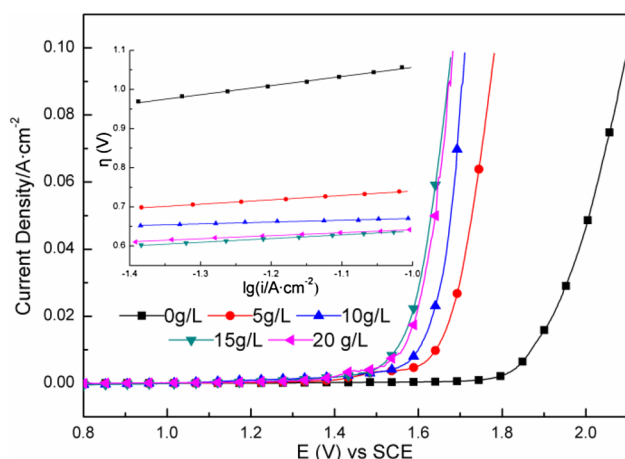


**Fig. 9** Anodic polarization curves for OERES electrodes in a simulation zinc electrowinning solution obtained from the original plating bath with different  $\text{Co}_3\text{O}_4$  concentrations; the Tafel lines in the OER potential range (inset)

particle closer to the substrate, and point 3 is positioned on the  $\beta\text{-PbO}_2$  deposition layer without core  $\text{Co}_3\text{O}_4$  particles. Comparing point 1 and point 2, the content of Co at point 1 is clearly higher than that at point 2, and the content of Pb at point 1 is lower, indicating a thinner  $\beta\text{-PbO}_2$  layer on the  $\text{Co}_3\text{O}_4$  particles farther away from the substrate. In addition, the fact that the particle size for the  $\beta\text{-PbO}_2$ -coated  $\text{Co}_3\text{O}_4$  farther away from the substrate is significantly smaller may confirm the possibility discussed above.

From the analysis above, several nucleation laws for the  $\beta\text{-PbO}_2\text{-Co}_3\text{O}_4$  layer can be obtained. In the  $\beta\text{-PbO}_2$  bath containing  $\text{Co}_3\text{O}_4$  particles, the electric field force plays a dominant role in the adsorption process for the  $\text{Co}_3\text{O}_4$  particles. Therefore, the circular cell boundaries for  $\alpha\text{-PbO}_2$  are the preferential adsorption regions for  $\text{Co}_3\text{O}_4$  particles. In addition, the nucleation of  $\beta\text{-PbO}_2$  on the substrate starts at the prominent position of the  $\alpha\text{-PbO}_2$  circular cell and gradually spreads to the cell boundaries. Finally, the nucleation and growth of  $\beta\text{-PbO}_2$  on the  $\text{Co}_3\text{O}_4$  particles started from the particles closer to the substrate. The thickness of the  $\beta\text{-PbO}_2$  layer on the  $\text{Co}_3\text{O}_4$  particles was inversely proportional to the distance between the  $\text{Co}_3\text{O}_4$  particles and the substrate.

Based on the composite electrodeposition mechanism (electrochemical mechanism [37–39]) and the previous analysis, in which the electric field force plays a dominant role, a nucleation model of the  $\beta\text{-PbO}_2\text{-Co}_3\text{O}_4$  deposition layer was developed, as shown in Fig. 8. The nucleation process for the  $\beta\text{-PbO}_2\text{-Co}_3\text{O}_4$  deposition layer can be divided into four steps: step 1: the  $\text{Co}_3\text{O}_4$  particles suspended in the  $\beta\text{-PbO}_2$  plating bath move from the depth of the plating solution to the vicinity of the substrate surface depending on the flow of the plating solution. Step 2: nucleation of  $\beta\text{-PbO}_2$  on the substrate starts at the prominent position of the  $\alpha\text{-PbO}_2$  circular cell and gradually spreads to the cell boundaries. The second step and the first step do not have a sequence and can be performed at the same time. Step 3: the  $\text{Co}_3\text{O}_4$  particles with anionic absorbents are electrophoretically pushed to the surface of the anode and adsorbed on the surface of the anode after reaching the double layer of the anode surface, which is mainly affected by the electric force. Due to the strong electric field at the depression of the circular cell boundaries of  $\alpha\text{-PbO}_2$ , the  $\text{Co}_3\text{O}_4$  particles preferentially move to this location and undergo adsorption at this location. Step 4: the  $\beta\text{-PbO}_2$  on the substrate continues to grow. At the same time,  $\beta\text{-PbO}_2$  nucleates on the adsorbed  $\text{Co}_3\text{O}_4$  particles, resulting in gradual but complete coating of the  $\text{Co}_3\text{O}_4$  particles with  $\beta\text{-PbO}_2$ .

### 3.3 OER property for the electrode

The  $\text{Co}_3\text{O}_4$  doped  $\beta\text{-PbO}_2$  electrodes were prepared in  $\beta\text{-PbO}_2$  baths with different  $\text{Co}_3\text{O}_4$  particle concentrations (0–20 g/L). The ultrasonic dispersion time for the  $\beta\text{-PbO}_2$  baths were controlled at 30 min. In addition, the temperature and time of the deposition process was controlled at 45 °C and 1 h, respectively. The anodic polarization curves for the OERES electrodes measured in a Zn electrowinning simulated system are shown in Fig. 9. The characteristics for the five anodic polarization curves are similar, with the current being almost zero before oxygen evolution and exponentially increasing after oxygen evolution, which are typical OER characteristic curves. With the doping of  $\text{Co}_3\text{O}_4$  particles, the initial oxygen evolution potentials for the electrodes were significantly reduced compared with the  $\beta\text{-PbO}_2$  electrodes without particles.

**Table 1** Kinetic parameters and overpotential for the OER at OERES electrodes in a simulation zinc electrowinning solution obtained from the original plating bath with varying  $\text{Co}_3\text{O}_4$  concentration

$\text{Co}_3\text{O}_4$ concentration (g/L)	Oxygen evolution overpotential $\eta/\text{V}$				$a$	$b$
	300 $\text{A m}^{-2}$	400 $\text{A m}^{-2}$	500 $\text{A m}^{-2}$	600 $\text{A m}^{-2}$		
0	0.934	0.963	0.986	1.004	1.289	0.233
5	0.681	0.695	0.706	0.715	0.852	0.112
10	0.645	0.651	0.656	0.660	0.717	0.047
15	0.588	0.600	0.609	0.617	0.733	0.095
20	0.602	0.611	0.619	0.625	0.719	0.077



Furthermore, the initial oxygen evolution potential shows a decreasing trend as the concentration of  $\text{Co}_3\text{O}_4$  increases in the  $\beta\text{-PbO}_2$  plating bath.

Figure 9b shows the Tafel lines ( $\eta = a + b \lg i$ ) in the OER potential range. The kinetic parameters for the Tafel linear fitting and OER overpotential at a current density of 300, 400, 500 and 600  $\text{mA}/\text{cm}^2$  are shown in Table 1. It can be found from Table 1 that the Tafel intercept ( $a$ ) and the Tafel slope ( $b$ ) are significantly reduced as the  $\text{Co}_3\text{O}_4$  particles are doped into the electrode. A smaller Tafel slope is more beneficial for energy-saving as it leads to a remarkably increased OER rate with an increase in overpotential [40–42]. When the  $\text{Co}_3\text{O}_4$  particle concentration in the plating bath is 15 g/L, the oxygen evolution overpotentials calculated at the different current densities were the lowest for the obtained electrode. Compared to the electrode prepared without  $\text{Co}_3\text{O}_4$  particles, the oxygen evolution overpotentials for the electrode at 300  $\text{A}/\text{m}^2$ , 400  $\text{A}/\text{m}^2$ , 500  $\text{A}/\text{m}^2$  and 600  $\text{A}/\text{m}^2$  are decreased by 346 mV, 363 mV, 377 mV, and 387 mV, respectively, which indicates an energy-saving effect. In addition, a further increase in the particle content in the plating solution will not contribute to an improved energy-saving effect.

## 4 Conclusions

In this study, the stability of a  $\text{Co}_3\text{O}_4$  suspension electrolyte was investigated by a Zeta potential test. The  $\beta\text{-PbO}_2$  bath containing  $\text{Co}_3\text{O}_4$  particles becomes more stable for an ultrasonic dispersion time within 30 min, with the stability beginning to decrease after the ultrasonic time exceeds 30 min.  $\text{Co}_3\text{O}_4$  particles in the  $\beta\text{-PbO}_2$  bath are positively charged, with anions being adsorbed onto the particles.

XRD, SEM, and EDS were utilized to investigate the nucleation of the composite layer. The electric field force plays a dominant role in the adsorption process for the  $\text{Co}_3\text{O}_4$  particles. Therefore, the circular cell boundaries of  $\alpha\text{-PbO}_2$  are a preferential adsorption region for  $\text{Co}_3\text{O}_4$  particles. In addition, the nucleation of  $\beta\text{-PbO}_2$  on the substrate starts at the prominent position of the  $\alpha\text{-PbO}_2$  circular cell and gradually spreads to the cell boundaries. The nucleation and growth of  $\beta\text{-PbO}_2$  on the  $\text{Co}_3\text{O}_4$  particles started for the particles closer to the substrate. In addition, the thickness of the  $\beta\text{-PbO}_2$  layer on the  $\text{Co}_3\text{O}_4$  particles was inversely proportional to the distance between the  $\text{Co}_3\text{O}_4$  particles and the substrate. Finally, the nucleation process for the  $\beta\text{-PbO}_2\text{-Co}_3\text{O}_4$  layer can be divided into four steps.

The influence of the  $\text{Co}_3\text{O}_4$  concentration on the electrode OER catalytic properties was characterized using anodic polarization curves. The oxygen evolution overpotential for the obtained electrode was the lowest for a

$\text{Co}_3\text{O}_4$  particle concentration of 15 g/L in the plating bath. Compared to the pure  $\text{PbO}_2$  electrode, the oxygen evolution overpotentials for the electrode at 300  $\text{A}/\text{m}^2$ , 400  $\text{A}/\text{m}^2$ , 500  $\text{A}/\text{m}^2$  and 600  $\text{A}/\text{m}^2$  are decreased by 346 mV, 363 mV, 377 mV, and 387 mV, respectively, which demonstrates an energy-saving effect.

**Acknowledgement** Authors gratefully acknowledge the financial supports of the National Natural Science Foundation of China (U1703130); the National Natural Science Foundation of China (Project No. 51874154); the Ministry of Education Key Laboratory Open Fund (Project No. KF17-09); the National Natural Science Foundation of China (Project No. 51564029); the Youth Foundation of Ahut (Project No. QZ201703).

## Compliance with ethical standards

**Conflict of interest** The authors declare that they have no competing interests.

## References

1. Tahir M, Pan L, Idrees F, Zhang X, Wang L, Zou JJ, Wang ZL (2017) Electrocatalytic oxygen evolution reaction for energy conversion and storage: a comprehensive review. *Nano Energy* 37:136–157
2. Kim JH, Youn DH, Kawashima K, Lin J, Lim H, Mullins CB (2018) An active nanoporous Ni(Fe) OER electrocatalyst via selective dissolution of Cd in alkaline media. *Appl Catal B Environ* 225:1–7
3. Singh A, Roy S, Das C, Samanta D, Maji TK (2018) Metallophthalocyanine based redox active metal-organic conjugated microporous polymers for OER catalysis. *Chem Commun* 54:4465–4468
4. Couper AM, Pletcher D, Walsh FC (1990) Cheminform abstract: electrode materials for electrosynthesis. *Cheminform* 21:837–865
5. Yang H, Chen B, Liu H, Guo Z, Zhang Y, Li X, Xu R (2014) Effects of manganese nitrate concentration on the performance of an aluminum substrate  $\beta\text{-PbO}_2\text{-MnO}_2\text{-WC-ZrO}_2$  composite electrode material. *Int J Hydrogen Energy* 39:3087–3099
6. Panizza M, Sir s I, Cerisola G (2008) Anodic oxidation of mecoprop herbicide at lead dioxide. *J Appl Electrochem* 38:923–929
7. Chang L, Zhou Y, Duan X, Liu W, Xu D (2014) Preparation and characterization of carbon nanotube and Bi co-doped  $\text{PbO}_2$ . *J Taiwan Inst Chem E* 45:1338–1346
8. Johnson DC, Feng J, Houk LL (2000) Direct electrochemical degradation of organic wastes in aqueous media. *Electrochim Acta* 46:323–330
9. An H, Li Q, Tao D, Cui H, Xu X, Ding L, Zhai J (2011) The synthesis and characterization of  $\text{Ti}/\text{SnO}_2\text{-Sb}_2\text{O}_3/\text{PbO}_2$  electrodes: the influence of morphology caused by different electrochemical deposition time. *Appl Surf Sci* 258:218–224
10. Xing J, Chen D, Zhao W, Zhao X, Zhang W (2015) Preparation and characterization of a novel porous  $\text{Ti}/\text{SnO}_2\text{-Sb}_2\text{O}_3\text{-CNT}/\text{PbO}_2$  electrode for the anodic oxidation of phenol wastewater. *RSC Adv* 6:53504–53513
11. Amadelli R, Armelao L, Velichenko AB, Nikolenko NV, Girenko DV, Kovalyov SV, Danilov FI (1999) Oxygen and ozone evolution at fluoride modified lead dioxide electrodes. *Electrochim Acta* 45:713–720
12. Wu J, Xu H, Yan W (2015) Fabrication and characterization of  $\beta\text{-PbO}_2/\alpha\text{-PbO}_2/\text{Sb-SnO}_2/\text{TiO}_2$  nanotube array electrode and its

- application in electrochemical degradation of Acid Red G. *RSC Adv* 25:19284–19293
13. Chen HY, Wu L, Ren C, Luo QZ, Xie ZH, Jiang X, Luo YR (2001) The effect and mechanism of bismuth doped lead oxide on the performance of lead–acid batteries. *J Power Sources* 95:108–118
  14. Moncada A, Mistretta MC, Randazzo S, Piazza S, Sunseri C, Inguanta R (2014) High-performance of PbO<sub>2</sub> nanowire electrodes for lead–acid battery. *J Power Sources* 256:72–79
  15. Moncada A, Piazza S, Sunseri C, Inguanta R (2015) Recent improvements in PbO<sub>2</sub> nanowire electrodes for lead-acid battery. *J Power Sources* 275:181–188
  16. Velayutham D, Noel M (1993) Effect of additives on the anodic codeposition of lead dioxide and polypyrrole. *J Appl Electrochem* 23:922–926
  17. Yang CJ, Park SM (2013) Electrochemical behavior of PbO<sub>2</sub> nanowires array anodes in a zinc electrowinning solution. *Electrochim Acta* 108:86–94
  18. Bode H (1977) Lead–acid batteries. Wiley, New York
  19. Devilliers D, Dinh T, Mahé E, Dauriac V, Lequeux N (2004) Electroanalytical investigations on electrodeposited lead dioxide. *J Electroanal Chem* 573:227–239
  20. Chen B, Guo Z, Huang H, Yang X, Cao Y (2009) Effect of the current density on electrodepositing alpha-lead dioxide coating on aluminum substrate. *Acta Metall Sin* 22:373–382
  21. He S, Xu R, Hu G, Chen B (2015) Study on the electrosynthesis of Pb–0.3%Ag/a-PbO<sub>2</sub> composite inert anode materials. *Electrochemistry* 83:974–978
  22. Jović BM, Lačnjevac UČ, Jović VD, Krstajić NV (2015) Kinetics of the oxygen evolution reaction on NiSn electrodes in alkaline solutions. *J Electroanal Chem* 754:100–108
  23. Surendranath Y, Kanan MW, Nocera DG (2010) Mechanistic studies of the oxygen evolution reaction by a cobalt–phosphate catalyst at neutral pH. *J Am Chem Soc* 132:16501–16509
  24. Wang X, Chen XY, Gao LS, Zheng HG, Zhang ZD, Qian YT (2004) One-dimensional arrays of Co<sub>3</sub>O<sub>4</sub> nanoparticles: synthesis, characterization, and optical and electrochemical properties. *J Phys Chem B* 108:16401–16404
  25. Yan Q, Li X, Zhao Q, Chen G (2012) Shape-controlled fabrication of the porous Co<sub>3</sub>O<sub>4</sub> nanoflower clusters for efficient catalytic oxidation of gaseous toluene. *J Hazard Mater* 209–210:385–391
  26. Yoon JW, Choi JK, Lee JH (2012) Design of a highly sensitive and selective C<sub>2</sub>H<sub>5</sub>OH sensor using p-type Co<sub>3</sub>O<sub>4</sub> nanofibers. *Sens Actuators, B* 161:570–577
  27. Takada S, Mikiko Fujii A, Kohiki S, Babasaki T, Deguchi H, Mitome M (2001) Intraparticle magnetic properties of Co<sub>3</sub>O<sub>4</sub> nanocrystals. *Nano Lett* 1:379–382
  28. Xu M, Fei W, Zhao M, Yang S, Song X (2011) Molten hydroxides synthesis of hierarchical cobalt oxide nanostructure and its application as anode material for lithium ion batteries. *Electrochim Acta* 56:4876–4881
  29. Wang G, Zhou S, Wang H, Ren Z, Bai J (2015) Preparation of carbon-coating layer by ethyne thermal decomposition and its effects on the improvement of lithium storage properties for Co<sub>3</sub>O<sub>4</sub> hexagonal micro-platelets. *Sci Adv Mater* 7:1272–1281
  30. Xiong L, Teng Y, Wu Y, Wang J, He Z (2014) Large-scale synthesis of aligned Co<sub>3</sub>O<sub>4</sub> nanowalls on nickel foam and their electrochemical performance for Li-ion batteries. *Ceram Int* 40:15561–15568
  31. Wang F, Lu CC, Qin Y, Liang CC, Zhao MS, Yang SC, Sun ZB, Song XP (2013) Solid state coalescence growth and electrochemical performance of plate-like Co<sub>3</sub>O<sub>4</sub> mesocrystals as anode materials for lithium-ion batteries. *J Power Sources* 235:67–73
  32. Yan N, Hu L, Li Y, Wang Y, Zhong H, Hu XY, Kong XK, Chen QW (2012) Co<sub>3</sub>O<sub>4</sub> nanocages for high-performance anode material in lithium-ion batteries. *J Phys Chem C* 116:7227–7235
  33. Dan Y, Lu H, Liu X, Lin H, Zhao J (2011) Ti/PbO<sub>2</sub> + nano-Co<sub>3</sub>O<sub>4</sub> composite electrode material for electrocatalysis of O<sub>2</sub> evolution in alkaline solution. *Int J Hydrogen Energy* 33:1949–1954
  34. Bertinello R, Furlanetto F, Guerriero P, Musiani M (1999) Electrodeposited composite electrode materials: effect of the concentration of the electrocatalytic dispersed phase on the electrode activity. *Electrochim Acta* 44:4061–4068
  35. Marsalek R (2014) Particle size and zeta potential of ZnO. *APCBEE Procedia* 9:13–17
  36. Tang X, Zheng H, Teng H, Zhao C, Wang Y, Xie W, Chen W, Yang C (2015) An alternative method for preparation of polyaluminum chloride coagulant using fresh aluminum hydroxide gels: characterization and coagulation performance. *Chem Eng Res Des* 104:208–217
  37. Thomas MA, Sun WW, Cui JB (2012) Mechanism of Ag doping in ZnO nanowires by electrodeposition: experimental and theoretical insights. *J Phys Chem C* 116:6383–6391
  38. Snaith DW, Groves PD (1972) Study of the mechanisms of cermet electrodeposition. *Trans Inst Met Finish* 50:95–101
  39. Zhou XW, Shen YF, Jin HM (2012) Microstructure and depositional mechanism of Ni–P coatings with nano-ceria particles by pulse electrodeposition. *Trans Nonferr Metals Soc China* 22:1981–1988
  40. Li Z, Yu XY, Paik U (2016) Facile preparation of porous Co<sub>3</sub>O<sub>4</sub> nanosheets for high-performance lithium ion batteries and oxygen evolution reaction. *J Power Sources* 310:41–46
  41. Song X, Yang T, Du H, Dong W, Liang Z (2016) New binary Mn and Cr mixed oxide electrocatalysts for the oxygen evolution reaction. *J Electroanal Chem* 760:59–63
  42. Abreu-Sepulveda M, Trinh P, Malkhandi S, Narayanan SR, Jorné J, Quesnel DJ, Manivannan A (2015) Investigation of oxygen evolution reaction at LaRuO<sub>3</sub>, La<sub>3.5</sub>Ru<sub>4</sub>O<sub>13</sub>, and La<sub>2</sub>RuO<sub>5</sub>. *Electrochim Acta* 180:401–408

**Publisher's Note** Springer Nature remains neutral with regard to jurisdictional claims in published maps and institutional affiliations.